# Mid-Pliocene West African Monsoon Rainfall as simulated in the PlioMIP2 ensemble

Ellen Berntell[1], Qiong Zhang[1], Qiang Li[1], Alan M. Haywood[2], Julia C. Tindall[2], Stephen J. Hunter[2],
Zhongshi Zhang[3,4], Xiangyu Li[3], Chuncheng Guo[4], Kerim H. Nisancioglu[4], Christian Stepanek[5,6], Gerrit
Lohmann[6], Linda E. Sohl[7,8], Mark A. Chandler[7,8], Ning Tan[9,10], Camille Contoux[10], Gilles Ramstein[10],
Michiel L. J. Baatsen[11], Anna S. von der Heydt[11,12], Deepak Chandan[13], William Richard Peltier[13], Ayako
Abe-Ouchi[14], Wing-Le Chan[14], Youichi Kamae[15], Charles J. R. Williams[16,17,18], Dan Lunt[16]

[1]Department of Physical Geography and Bolin Centre for Climate Research, Stockholm University, Stockholm, Sweden
[2]School of Earth and Environment, University of Leeds, Woodhouse Lane, Leeds, West Yorkshire, UK
[3]Department of Atmospheric Science, School of Environmental Studies, China University of Geosciences, Wuhan, China
[4]NORCE Norwegian Research Centre, Bjerknes Centre for Climate Research, Bergen, Norway
[5]Institute for Environmental Physics, University of Bremen, Bremen, Germany
[6]Alfred Wegener Institute - Helmholtz-Zentrum für Polar und Meeresforschung, Bremerhaven, Germany
[7]Center for Climate Systems Research, Columbia University, New York, USA
[8]NASA Goddard Institute for Space Studies, New York, USA
[9]Key Laboratory of Cenozoic Geology and Environment, Institute of Geology and Geophysics, Chinese Academy of Sciences,
Beijing, China
[10]Laboratoire des Sciences du Climat et de l'Environnement, LSCE/IPSL, CEA-CNRS-UVSQ, Université Paris-Saclay, Gif-
sur-Yvette, France
[11]Centre for Complex Systems Science, Utrecht University, Utrecht, The Netherlands
[12]Institute for Marine and Atmospheric research Utrecht (IMAU), Department of Physics, Utrecht University, Utrecht, The
Netherlands.
[13]Department of Physics, University of Toronto, Toronto, Ontario, Canada
[14]Centre for Earth Surface System Dynamics (CESD), Atmosphere and Ocean Research Institute (AORI), University of Tokyo,
Tokyo, Japan
[15]Faculty of Life and Environmental Sciences, University of Tsukuba, Tsukuba, Japan
[16]School of Geographical Sciences, University of Bristol, Bristol, UK
[17]NCAS-Climate, University of Reading, Reading, UK
[18]Department of Meteorology, University of Reading, Reading, UK

*Correspondence to*: Ellen Berntell (ellen.berntell@natgeo.su.se)

**Abstract.** The mid-Pliocene Warm Period (mPWP; ~3.2 million years ago) is seen as the most recent time period characterized by a warm climate state, with similar modern geography and ~400 ppmv atmospheric $CO_2$ concentration, and is therefore often considered an interesting analogue for near-future climate projections. Paleoenvironmental reconstructions indicate higher surface temperatures, decreasing tropical deserts, and a more humid climate in West Africa characterized by a strengthened West African Monsoon (WAM). Using model results from the second phase of the Pliocene Modelling Intercomparison Project (PlioMIP2) ensemble we analyze changes of the WAM rainfall during the mPWP, by comparing with the control simulations for the pre-industrial period. The ensemble shows a robust increase of the summer rainfall over West Africa and the Sahara region with an average increase of 2.7 mm/day, contrasted by a rainfall decrease over the equatorial Atlantic. An anomalous warming of the Sahara Desert and deepening of the Saharan Heat Low, seen in >90% of the models, leads to a strengthening of the WAM and an increased monsoonal flow into the continent. A similar warming of the Sahara Desert is seen in future projections using both phase 3 and 5 of the Coupled Model Intercomparison Project (CMIP3 and CMIP5), and though previous studies of future projections indicate a west/east drying/wetting contrast over Sahel, PlioMIP2 simulations indicate a uniform rainfall increase over Sahel in warm climates characterized by increasing greenhouse gas forcing.

## 1. Introduction

The mid-Pliocene Warm Period (mPWP; 3.264-3.025 Ma; also known as the mid-Piacenzian Warm Period) is considered to be the most recent historical warm climate state, with average global temperatures several degrees above pre-industrial (PI) levels (1.4 - 4.7 °C; Haywood et al., 2020) and atmospheric $CO_2$ concentrations of ~400 ppmv (Badger et al., 2013; Bartoli et al., 2011; Dowsett et al., 2010; Haywood et al., 2020, 2013; Martínez-Botí et al., 2015; Pagani et al., 2010; Raymo et al., 1996; Salzmann et al., 2013; Seki et al., 2010; Tripati et al., 2009; Zhang et al., 2013). Paleoenvironmental reconstructions indicate a warm and humid climate during the mPWP, with elevated sea surface temperatures (SSTs) and surface air temperatures (SATs), especially at high latitudes (Dowsett et al., 2010; Salzmann et al., 2013), forests and grassland expanding into areas previously covered by tundra, and savanna and woodland expanding at the expense of deserts (Salzmann et al., 2008). While much of the research on the mPWP climate focused on global large-scale patterns and the high latitudes (Haywood et al., 2013, 2020; De Nooijer et al., 2020), several studies have emphasized the implications of the warm climate state for tropical climate, showing e.g. an enhancement of the East Asian Summer Monsoon (Wan et al., 2010) and a drying of the Southern Hemisphere tropics and subtropics (Pontes et al., 2020). Analysis of e.g. dust records of the coast of West Africa also indicates a strengthened West African Monsoon (WAM) during the mPWP as well as wetter conditions over West Africa and the Sahara region (Kuechler et al., 2018; Salzmann et al., 2008).

With a paleogeography and atmospheric $CO_2$ concentrations similar to today (Dowsett et al., 2010), the mPWP has long been considered an interesting analogue for near-future climate projections (Chandler et al., 1994; Jiang et al., 2005) and been the focus of many modelling studies (e.g. Haywood and Valdes, 2004; Salzmann et al., 2008). To increase our understanding of the dynamical drivers of the warm climate state, several model simulations have been performed as part of the Pliocene Modelling Intercomparison Project (PlioMIP; Haywood et al., 2010, 2011). Model-data comparisons between the PlioMIP1 (first phase of PlioMIP) simulations and PRISM3 reconstructions (Dowsett et al., 2010) have shown an underestimation of the high-latitude warming in the mPWP and an overestimation of the warming in the Tropics (Haywood et al., 2013; Salzmann et al., 2013), which has influenced the representation of the WAM within the models (Zhang et al., 2016). PlioMIP1 was later followed up by a second phase (PlioMIP2), representing a more narrow geological time-window (marine isotope stage KM5c, 3.205 Mya) to e.g. facilitate data-model comparison (Haywood et al., 2016), and though some areas of concern still remain, results from the PlioMIP2 have shown a widespread model-data agreement (Haywood et al., 2020).

While previous studies have shown that the high-latitude warming has reduced the equator-pole temperature gradient (Haywood et al., 2013) and weakened tropical circulation such as the Hadley Circulation (Corvec and Fletcher, 2017), the terrestrial warming during the mPWP has been shown to strengthen the WAM and increase the summer rainfall over the Sahel region by more than 1 mm/day (Haywood et al., 2020; Zhang et al., 2016). A similar rainfall increase over Sahel is seen in future projections for both CMIP3 and CMIP5 ensembles, though with a drying located over western Sahel (Roehrig et al., 2013). However, models have been shown to inaccurately capture rainfall variability and change over West Africa and the Sahel region (Berntell et al., 2018; Roehrig et al., 2013), and there is still little confidence in future projections of the summer rainfall (Biasutti et al., 2008; Cook, 2008; Roehrig et al., 2013). West Africa is a region sensitive to hydrological variability which experienced extended droughts during the 1970s and 1980s (Berntell et al., 2018; Held et al., 2005; Nicholson et al., 2000), and there is a large need to increase the confidence in future projections in order to support adaption strategies in the region.

The similarity to modern conditions, as well as the high amount of paleogeological and environmental data from the mPWP, has made it well suited to both evaluate the models' ability to capture a warm climate state and further our understanding of the effects of greenhouse gas forcing on the global climate system (Haywood et al., 2020; Haywood and Valdes, 2004). In this article we will evaluate the representation of the WAM within the PlioMIP2 ensemble, qualitatively compare it to palaeohydrological reconstructions and discuss the implications for the WAM in a near-future warm climate state with increasing greenhouse gas forcing.

## 2. Data and method

### 2.1. Participating PlioMIP2 models

To examine the behavior of the WAM during the mPWP, data produced by 17 different general circulation models as part of the PlioMIP2 was used (Table 1). Simulations produced within PlioMIP2 are run for at least 500 years (Haywood et al., 2016) towards an equilibrium state, and the last 100 years of the simulations are then used for analysis. In the experimental set-up the $CO_2$ levels are set to 400 ppmv, and the remaining concentrations of trace gases and aerosols are set to pre-industrial levels (Haywood et al., 2016). The simulations are run using enhanced boundary conditions as described in Haywood et al., (2016), with changes to e.g. the topography, bathymetry and land ice cover. COSMOS uses dynamic vegetation (Stepanek et al., 2020), while the remaining 16 models use

100    prescribed vegetation based on Salzmann et al. (2008). As the models have different horizontal resolutions, the

data from the models was bilinearly interpolated onto a 1º x 1º grid using the software CDO (Climate Data

Operators, Schulzweida, 2019) to facilitate multi-model analysis.

**Table 1: PlioMIP2 models used in this study. Spatial resolution of the atmosphere model indicated by grid cell extent (in degrees longitude x latitude) and number of vertical layers (L).**

| Model ID | Atmospheric resolution | Reference |
|---|---|---|
| CCSM4-NCAR | 1.25 x 0.9, L26 | Feng et al. (2020) |
| CCSM4-Utrecht | 2.5 x 1.9, L26 | |
| CCSM4-UofT | 1.25 x 0.9, L26 | Chandan and Peltier (2017) |
| CESM1.2 | 1.25 x 0.9, L30 | Feng et al. (2020) |
| CESM2 | 1.25 x 0.9, L32 | Feng et al. (2020) |
| COSMOS | T31 (~3.75 x 3.75), L19 | Stepanek et al. (2020) |
| EC-Earth3-LR | T159 (~1.125 x 1.125), L62 | Zhang et al. (in review) |
| GISS-E2-1-G | 2.0 x 2.5, L40 | Chandler et al. (in prep.) |
| HadCM3 | 2.5 x 3.75, L19 | Hunter et al. (2019) |
| HadGEM3(-GC31-LL) | N96 (~1.875 x 1.25), L85 | Williams et al. (2018) |
| IPSLCM6A-LR | 2.5 x 1.26, L79 | Lurton et al. (2020) |
| IPSLCM5A2 | 3.75 x 1.9, L39 | Tan et al. (2020) |
| IPSLCM5A | 3.75 x 1.9, L39 | Tan et al. (2020) |
| MIROC4m | T42 (~2.8 x 2.8), L20 | Chan et al. (2020) |
| MRI-CGCM 2.3 | T42 (~2.8 x 2.8), L30 | Kamae et al. (2016) |
| NorESM-L | T31 (~3.75 x 3.75), L26 | Li et al. (2020) |
| NorESM1-F | 1.9 x 2.5, L26 | Li et al. (2020) |

105

2.3 Method

The rainfall is analyzed over the months July-September (JAS), and the multi-model mean (MMM) represents the

un-weighted average of the PlioMIP2 ensemble. The robustness of the signal is evaluated using the methodology

of Mba et al. (2018), where the signal is considered robust if at least 14 of the 17 models agree on the sign of the

110    anomaly (=>80%) and the MMM anomaly is equal to or larger than the inter-model standard deviation. The models

are evaluated against their PI-simulation, and the 1901-1930 climatology based on CRU TS v4 (Climatic Research

Unit gridded Time Series; Harris et al., 2020) is included as a reference for the observations. The seasonal cycle of

the WAM is also examined over two sub-regions, Sahel (10-20° N, 20° W-30° E) and the Coast of Guinea (5-10°

N, 20° W-30° E), representing regions characterized by a narrow and a wider or bimodal rainfall season

115    respectively.

3. Results

3.1. Changes in seasonality
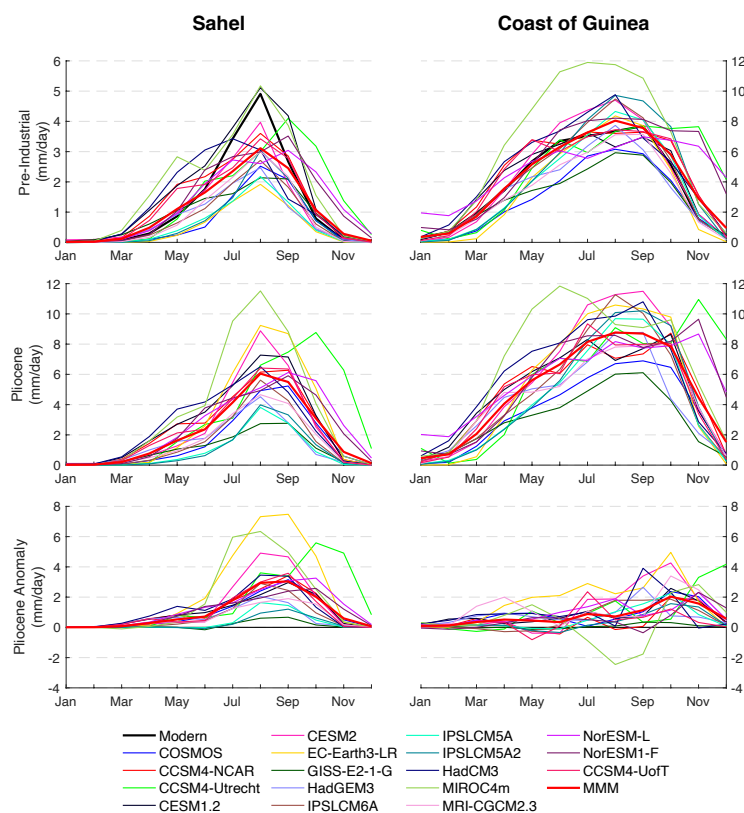
**Fig. 1: Seasonal cycle of rainfall (unit: mm/day) over Sahel (left) and the Coast of Guinea (right) for PI (top),**

120      **mPWP (center) and mPWP anomalies (mPWP-PI, bottom). The multi-model mean MMM is shown together**

**with the individual models, and the modern conditions as derived from observations (Harris et al., 2020) are**

**included as a reference.**

The progression of the WAM creates different seasonal cycles of rainfall depending on the region, where northern

latitudes in West Africa have one clear peak while more southern regions have a wider or bimodal rainy season.

125      We have therefore divided West Africa into two sub-regions, Sahel (10-20° N, 20° W-30° E) and Coast of Guinea

(5-10° N, 20° W-30° E). The seasonal cycle of terrestrial rainfall is calculated for each ensemble member and

presented together with the MMM for the PI and mPWP simulations separately, as well as for the Pliocene anomaly

(mPWP-PI) (Fig. 1). The "modern" seasonal cycle is plotted together with the PI cycle for reference, based on

1901-1930 CRU TS v4 data (Harris et al., 2020).

130    In agreement with PI observations, the PI MMM shows a seasonal cycle with an August peak in rainfall over Sahel at 3.1 mm/day. The individual models mainly exhibit the same seasonal cycle; however, four models exhibit highest levels of rainfall shifted to July (HadCM3) or September (CCSM4-Utrecht, NorESM-L and NorESM-F) rather than August. The magnitude of summer rainfall seen in CESM1.2 and MIROC4m is at 5.1 and 5.2 mm/day respectively comparable to modern conditions (Fig. 1), while the other 15 ensemble members remain within a span of 2-4

135    mm/day which is considerably below modern levels. The mPWP MMM shows an increase in monsoon rainfall, with the maximum rainfall doubling and reaching 6.1 mm/day in August. All models show an increase in rainfall in the July-October period, with the largest increase occurring either in August, September or October, resulting in a lengthening of the WAM. Keeping with previous studies (e.g. Berntell et al., 2018; Giannini et al., 2003; Mohino et al., 2011; Roehrig et al., 2013), we will however still base our spatial analysis of the WAM on the July-September

140    period. The largest increase is shown in EC-Earth3-LR at 7.3 and 7.5 mm/day in August and September, making it reach a maximum of 9.2 mm/day in Pliocene Sahel. As with the PI, the highest level of Pliocene rainfall in the PlioMIP2 ensemble is seen in MIROC4m with 11.5 mm/day in August.

Over the Coast of Guinea, the PI simulations show higher levels of rainfall through most of the Northern Hemispheres spring, summer and fall, with the ensemble mean showing a maximum of 8.1 mm/day occurring in

145    August (Fig. 1). 16 of the 17 members have maximum levels of rainfall spanning between 5.9 mm/day and 9.8 mm/day, while MIROC4m again supersedes the remaining models with rainfall reaching 11.9 mm/day in July. The MMM of the mPWP simulations again shows an increase of monsoon rainfall compared to the PI, with positive anomalies throughout the seasonal cycle but showing highest values in October and a secondary peak in July. However, while no individual models showed negative anomalies during the monsoon season in Sahel, CCSM4-

150    NCAR, MIROC4m and NorESM1-F show decrease in rainfall over the Coast of Guinea in July-September. The remaining models show both increasing and decreasing rainfall during April-June, but mainly positive anomalies from July-November.

3.2. Changes in monsoon rainfall
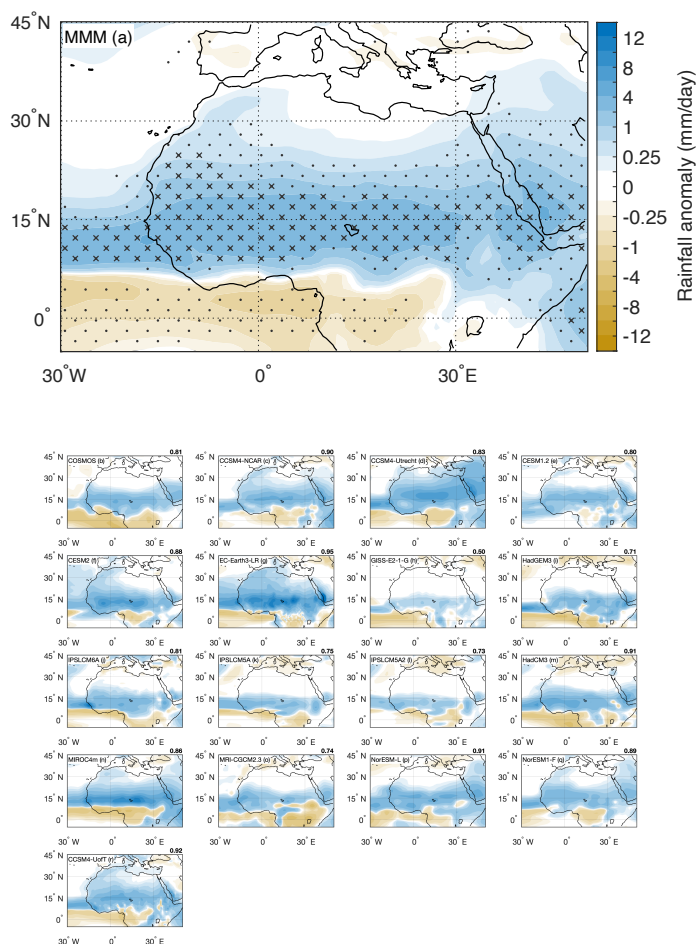
**Fig 2. mPWP July-August-September (JAS) rainfall anomalies (mPWP-PI) for the MMM (a) and the individual models**

155 **(b-r), with all subfigures using the same color bar. Robust signals are indicated with x, where ~80% of the models (14 out of 17) show the same sign of anomaly and the anomaly is equal to or larger than the inter-model standard deviation, and dots indicate that only the first criterion is fulfilled. The pattern correlation between the MMM and individual model is seen in top right corner.**

To see the changes in the WAS rainfall during the mPWP we look at the JAS rainfall anomalies (mPWP-PI, Fig.

160 2). The MMM shows a clear dipole pattern with a latitudinal transition at 7°N stretching from the Atlantic Ocean to the eastern part of Northern Africa (Fig. 2a). The robust signal of rainfall increase is centered on Sahel and southern Sahara, covering most of northern Africa and reaching from the Coast of Guinea into northern Sahara.

The negative anomalies cover an area stretching from 7°N and continuing south over the Equatorial Atlantic, with the largest decrease located along the Gulf of Guinea.

165    The large-scale features of the rainfall anomalies are consistent over the individual models, with the rainfall increase centered at 10-15° N and reaching up into southern Sahara, and negative values located over the Gulf of Guinea (Fig. 2a and 2b-r). The results are less consistent along the Coast of Guinea with models indicating slightly different locations of the transition from negative to positive rainfall anomalies. Some models exhibit a rainfall decrease reaching up to 9°N (MIROC4m, GISS-E2-1-G) while other models limit the negative values to only cover

170    the Equatorial Atlantic and Central Africa (CCSM4-UoT, HadCM3). EC-Earth3-LR and CCSM-UofT show the highest pattern correlation to the MMM at $R$=0.95 and $R$=0.92 respectively, while GISS-E2-1-G has the lowest correlation ($R$=0.50). The different models show the largest spread over Sahel and southern Sahara (standard deviation of 2-4 mm/day, not shown). This is a region where all models indicate an increase in rainfall, but the simulated magnitude differs largely, from over 8 mm/day in EC-Earth3-LR and MIROC4m to around 1 mm/day

175    for GISS-E2-1-G and IPSLCM5A2. A spatial mean of the rainfall anomalies over Sahel (Fig. 3) shows a similar spread, with the highest values for EC-Earth3-LR and MIROC4m (6.6 and 5.8 mm/day) and the lowest for GISS-E2-1-G and IPSLCM5A2 (0.5 and 0.8 mm/day). The remaining 13 models all show an increase of 1-4 mm/day over Sahel with a MMM of 2.7 mm/day.
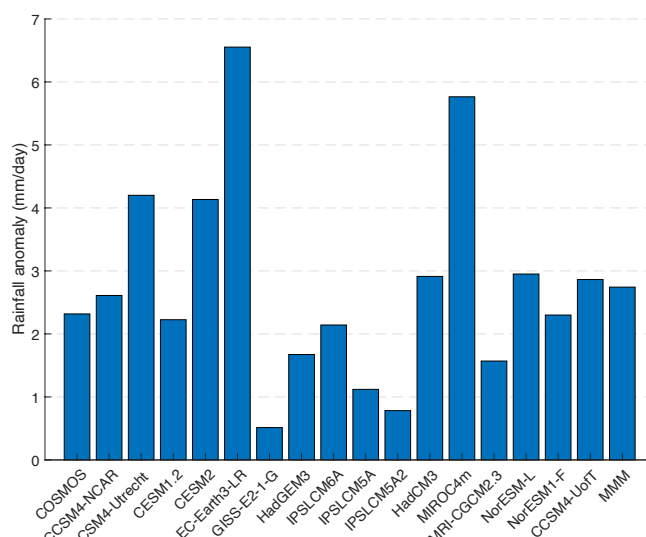
**Fig. 3. Mean July-September (JAS) Sahel mPWP rainfall anomaly (mPWP-PI, unit: mm/day) for the individual**

180    **PlioMIP2 ensemble models, together with the MMM.**

Looking at the latitudinal mean JAS rainfall (Fig. 4) we can also see that the rainbelt, i.e. the latitudinal band of maximum rainfall during the WAM, has shifted northward in the mPWP and is centered at 9.5°N with the largest rainfall increase of 2.0 - 3.4 mm/day occurring between 9.5°N and 17.5°N for the MMM. The ensemble does

185 however still exhibit a large spread, with four models showing a maximum increase to the south of the MMM (GISS-E2-1-G, IPSLCM5A, IPSLCM5A2 and IPSLCM6A) and two models showing a substantially larger increase than the MMM (EC-Earth3-LR and MIROC4m).
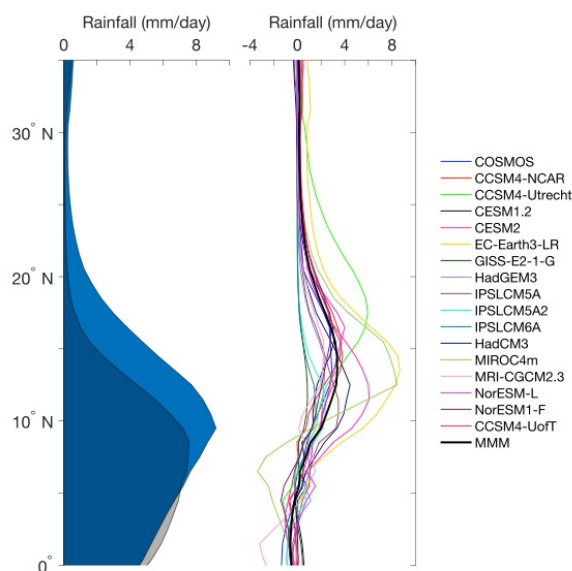
**Fig. 4. (left) Latitudinal mean terrestrial rainfall for MMM PI (grey) and mPWP (blue), with dark blue where they**
**overlap, and (right) latitudinal mean July-September (JAS) rainfall anomalies (mPWP-PI) for the individual models**
190 **and for the MMM.**

3.3. The dynamics for the changes in WAM rainfall

To understand the dynamics behind the increased rainfall in West Africa during the mPWP, the sea level pressure, horizontal wind at 850 hPa and near surface temperature anomalies (mPWP-PI) are analyzed for each individual model.
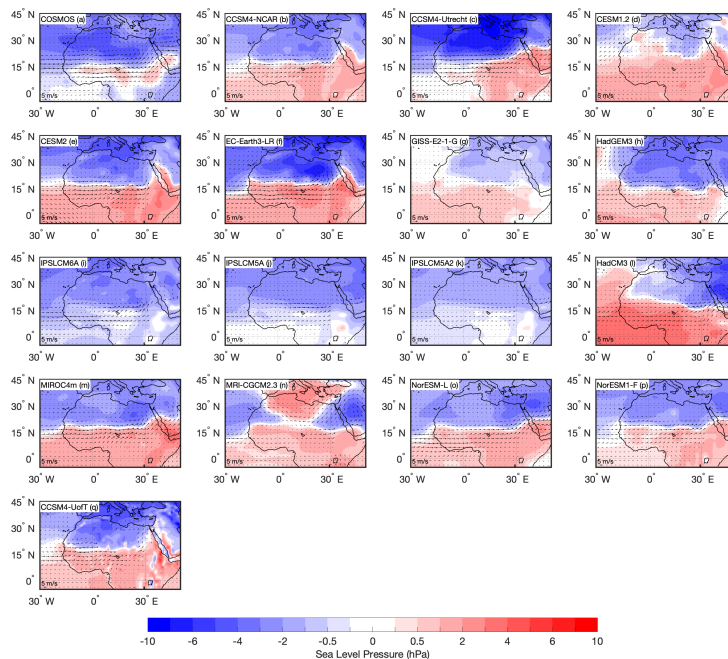
**Fig. 5. July-September (JAS) mean sea level pressure (shading) and 850 hPa horizontal wind (vectors) anomalies for the PlioMIP2 ensemble members (a-q).**

Sea level pressure anomalies for the monsoon season (JAS, mPWP-PI) are shown in Fig. 5 for the individual PlioMIP2 models. All models except MRI-CGCM 2.3 (Fig. 5n) show a deepening of the low-pressure area across the Sahara region (negative anomalies) and a strengthening of the negative latitudinal pressure gradients between Sahara and the Equatorial Atlantic. EC-Earth3-LR and CCSM4-UofT (Fig. 5f and 5q), the models with the highest pattern correlation in rainfall to the ensemble mean, both exhibit a clear north/south dipole pattern with negative sea level pressure anomalies over Sahara continuing northward into Europe, and positive anomalies over Sahel, the Coast of Guinea and the Equatorial Atlantic. The same dipole pattern, with a latitudinal transition at approx. 17°N, is also seen in nine additional ensemble members (CCSM4-NCAR, CCSM4-Utrecht, CESM2, GISS-E2-1-G, HadGEM3, HadCM3, MIROC4m, NorESM-L and NorESM1-F), but while MRI-CGCM 2.3 exhibits positive sea level pressure anomalies south of 15°N, the negative anomalies over Sahara are divided by positive anomalies over northern Africa and southern Europe, centered on the Mediterranean region, resulting in a quadrupole-type pattern (Fig. 5n). The three IPSL models (IPSLCM6A, IPSLCM5A and IPSLCM5A2) show negative anomalies or weak positive anomalies south of 17°N, forming a weaker enhancement of the latitudinal pressure gradient relative to the other PlioMIP2 models.

Associated with the deepening of the Saharan Heat Low and strengthening of the latitudinal pressure gradients is

an anomalous cyclonic flow and strengthened westerly/southwesterly horizontal winds at the 850 hPa level, going

from the Equatorial Atlantic into Sahel and Sahara (Fig. 5 a-q). This is seen in all models, although at different

magnitudes, with the highest increase in wind speed seen in CCSM4-Utrecht, EC-Earth3-LR and MIROC4m (Fig.

215    5c, 5f and 5m), and the lowest increase for GISS-E2-1-G, IPSLCM5A and IPSLCM5A2 (Fig. 5g, 5j and 5k).
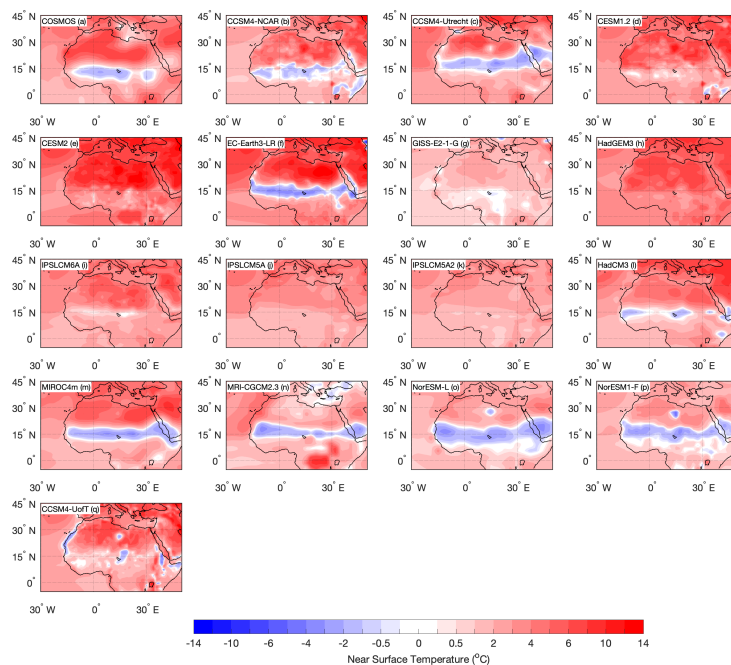
**Fig. 6. July-September (JAS) mean near surface temperature anomalies (ΔSAT, mPWP-PI) for the PlioMIP2 ensemble**

**members (a-q).**

The JAS near surface temperature anomalies (ΔSAT, mPWP-PI, Fig. 6) shows a strengthened north-south

temperature gradient between the Sahara Desert and the Equatorial Atlantic for all models except MRI-CGCM 2.3

220    (Fig. 6n). The temperature increase either stretches relatively uniformly across Sahara as in EC-Earth3-LR,

COSMOS and CCSM4-UoT, or exhibits two separate centers, one in Western Sahara and one in Eastern Sahara,

as for MIROC4m, NorESM-L and NorESM1-F. MRI-CGCM 2.3 (Fig. 6n) has positive temperature anomalies

located mainly outside Sahara, both centered along the western coast of Sahara and over eastern Sahara and the

Arabian peninsula. An area of negative temperature anomalies is located over the Mediterranean region, and its

225    surrounding areas in northern Sahara exhibit a weaker warming than the neighboring areas of the Sahara Desert.

Nine models show clear latitudinal bands of negative anomalies anomalies stretching across northern Africa at

approx. 15°N (COSMOS, CCSM4-NCAR, CCSM4-Utrecht, EC-Earth 3-LR, HadCM3, MIROC4m, MRI-CGCM 2.3, NorESM-L, NorESM1-F), similar to the latitude of maximum rainfall increase. GISS-E2-1-G and CCSM4-UoT exhibit negative anomalies more dispersed over northern Africa, located mainly along the western coastline

230   of Sahara and over the central Sahel region.

## 4. Discussion

### 4.1 The paleo-proxy evidence for WAM during the mid-Pliocene

The mid-Pliocene Warm Period is often used as an analog for near-future climate change due to its similar-to-modern paleogeography and high concentrations of $CO_2$ in the atmosphere (Corvec and Fletcher, 2017; Dowsett et

235   al., 2013; Sun et al., 2013), and both marine and terrestrial proxy reconstructions indicate a climate with higher sea surface and surface air temperatures than present (Dowsett et al., 2013; Salzmann et al., 2008). Model/data comparison using PlioMIP1 indicated that the models underestimated the high latitude warming by up to 15 °C while overestimating the low latitude temperatures by 1-6 °C (Dowsett et al., 2013; Haywood et al., 2013; Salzmann et al., 2013). A comparison of atmosphere-only general circulation models (AGCM) and coupled ocean-atmosphere

240   models (AOGCM) showed that AGCMs using prescribed SSTs based on paleo reconstructions produce a much stronger WAM compared to models using a coupled ocean-atmosphere configuration, believed to be due to the overestimation of SST and SAT in the tropics in the AOGCM's (Zhang et al., 2016). Analysis of the PlioMIP2 ensemble by Haywood et al. (2020) indicates a widespread model/data agreement for SSTs and little systematic temperature bias in the tropics, suggesting a reduced underestimation of the WAM in the PlioMIP2, but the

245   relatively low availability of palaeohydrological proxies covering West Africa makes it difficult to perform a similar model/data comparison for the WAM and its related rainfall (Salzmann et al., 2008, 2013). However, several studies of proxy reconstructions across Northern Africa indicates a more humid climate during the mid-Pliocene. Palynological data records indicate a higher density of tree cover and an expansion of woodland and savanna in Northern Africa at the expense of deserts (Bonnefille, 2010; Salzmann et al., 2008) and multi-proxy

250   studies analyzing e.g. plant-wax and dust records in marine sediment cores taken off-shore of West Africa indicate wetter conditions during the mid-Pliocene (deMenocal, 2004; Feakins et al., 2005; Kuechler et al., 2018), which is qualitatively consistent with the results from the PlioMIP2 ensemble (Fig. 2). The expansion of forest into the Sahara region is also seen in the results from COSMOS (Stepanek et al., 2020), which is the only member of the

PlioMIP2 ensemble that is run with dynamic vegetation. It is also important to note that the PlioMIP2 ensemble is

255    designed to simulate the MIS KM5c within the mPWP (Haywood et al., 2020, 2016), and while it represents a

useful comparison to modern conditions it might not represent the full climate variability within the mPWP,

possibly affecting model-data comparisons (Samakinwa et al., 2020).

## 4.2 WAM – PI and mid-Pliocene

| COSMOS | CCSM4-NCAR | CCSM-Utrecht | CESM1.2 | CESM2 | EC-Earth3-LR | GISS-E2-1-G | HadGEM3 | IPSLCM5A2 | IPSLCM5A | IPSL-CM6A-LR | HadCM3 | MIROC4m | MRI-CGCM2.3 | NorESM1-F | NorESM-L | CCSM4-UoT |
|---|---|---|---|---|---|---|---|---|---|---|---|---|---|---|---|---|
| 0.95 | 0.98 | 0.97 | 0.96 | 0.98 | 0.90 | 0.95 | 0.95 | 0.93 | 0.90 | 0.93 | 0.95 | 0.96 | 0.94 | 0.97 | 0.96 | 0.97 |

**Table 2. Pattern correlation of July-September mean rainfall over West Africa (0-25° N, 30° W-30° E) between**

260    **PlioMIP2 PI simulations and observational data (CRU TS v4.: 1901-1930 mean).**

High pattern correlations of JAS rainfall over West Africa ($R>0.90$; Table 2) between the PI simulations and

climatologies based on observational data (CRU: 1901-1930 (Harris et al., 2020)) for all models indicate that the

models are able to sufficiently reproduce the WAM rainfall pattern. However, looking at the absolute values (Fig.

1) it is clear that while they capture the general seasonal cycle with rainfall peaking in July-September, most models

265    still underestimate the magnitude of the modern summer rainfall over Sahel by 1-3 mm/day, the only exceptions

being CESM1.2 and MIROC4m with >5 mm/day of rainfall in August. This is consistent with our general

understanding that models struggle to capture West African rainfall (e.g. Roehrig et al., 2013).

The MMM shows a clear increase in summer rainfall in the Sahel region, consistent with a strengthened WAM

during the mPWP (Fig. 1). The anomalies are centered on mid to late summer (August-September), which indicates

270    a later withdrawal of the WAM and a lengthened monsoon season. The monsoonal rainfall over the (terrestrial)

Coast of Guinea also exhibits larger positive anomalies over the later months of the summer rainfall, further

suggesting an intensification of the WAM rainfall towards the end of the monsoon season as well as a later

withdrawal during the mid-Pliocene.

There is a large consistency within the ensemble regarding the general features of the mPWP WAM (Fig. 2). All

275    models are showing a JAS rainfall increase over Sahel reaching up into Sahara, and negative anomalies over the

Equatorial Atlantic, indicating an intensification and northward shift as well as expansion of the WAM. The

changes are statistically robust and consistent with previous studies on both PlioMIP1 and 2 where the tropics, particularly the Northern Hemisphere monsoon regions, are identified as a region with a robust rainfall signal during the mid-Pliocene (Haywood et al., 2020; Li et al., 2018; Pontes et al., 2020; Zhang et al., 2016). The signal

280    is markedly stronger in the PlioMIP2 compared to PlioMIP1, where the MMM shows a doubling of the rainfall increase over Sahel from 1-2 mm/day in PlioMIP1 (Zhang et al., 2016) to 2-4 mm/day in PlioMIP2 (Fig. 2), although the use of June-August as the monsoon season in Zhang et al. (2016) might also have contributed to the discrepancy, especially given the rainfall increase seen over the later part of the monsoon season (Fig 1). The weakest rainfall increase in Sahel is seen in GISS-E2-1-G (Fig 2), which is consistent with the model's low global

285    rainfall response to the $CO_2$ changes (Haywood et al., 2020). Models which were identified as having a larger land/sea rainfall anomaly contrast with a larger rainfall enhancement over land compared to the ocean (Haywood et al., 2020), are also the models which show a larger rainfall increase in Sahel (EC-Earth3-LR, HadCM3, MIROC4m, NorESM1-F, NorESM-L and CCSM4-UoT). However, COSMOS, which did not show a clear land enhancement globally, exhibits similar levels of rainfall increase in Sahel, and even slightly more than NorESM1-

290    F (2.32 and 2.30 mm/day respectively).

Haywood et al. (2020) also suggests that, in general, models exhibiting large SAT sensitivity (i.e., high global mean ΔSAT) also exhibit a larger rainfall change (globally), but there is still uncertainty in changes in more regional patterns. While it is consistent with the results from EC-Earth3-LR, which has both one of the highest increase in Sahel rainfall and global SAT (De Nooijer et al., 2020), there is less consistency within the remaining ensemble.

295    MIROC4m and IPSLCM6A both exhibit similar global ΔSAT (De Nooijer et al., 2020), but their rainfall change differs by close to a factor of 3 (Fig. 3). The PlioMIP2 models however show a consistent JAS warming of the Sahara Desert (Fig. 6), and if the region is limited to the Sahara (10°W-10°E, 20-30°N) a clear link between the ΔSAT and the rainfall increase can be observed (*R*=0.50, 95% significance). The warming of the Sahara Desert and strengthened latitudinal temperature gradient between the Sahara region and the equatorial Atlantic leads to a

300    deepening of the thermally induced Saharan Heat Low (Fig. 5) (Lavaysse et al., 2009). This deepened Saharan Heat Low induces low-level convergence and strengthens the southwesterly flow, bringing moisture from the equatorial Atlantic into the continent, leading to increased moisture availability and rainfall over Sahel and parts of Sahara and indicating a strengthened WAM (Fig. 5).

**Climate of the Past** Open Access
**Discussions**
EGU

The warming of the Sahara region and subsequent strengthening of the WAM is similar to what we see during other

305 warm climates, such as the Mid-Holocene and Last Interglacial period (Gaetani et al., 2017; Otto-Bliesner et al., 2020), but given the boundary conditions in the mid-Pliocene simulations this warming over Sahara is most likely due to the changes in the atmospheric $CO_2$-concentration. Studies of model simulations as well as observational data has shown that greenhouse gas forcing leads to a land-ocean warming contrast, with a larger temperature increase over land (Byrne and O'Gorman, 2013; Haywood et al., 2020; Lambert et al., 2011). The contrast is a

310 result of the lower moisture availability over land influencing the lapse rate and leading to a higher warming compared to the ocean (Byrne and O'Gorman, 2013), which is consistent with the strong response over the arid Sahara region (Fig. 6). Studies show that this land/ocean warming contrast is present in both equilibrium and transient simulations (Lambert et al., 2011), and future scenarios of climate change show a continued land/ocean contrast and warming of the Sahara region (Boer, 2011; Sutton et al., 2007), leading to strengthened latitudinal

315 temperature gradients.

The enhanced vegetation over West Africa in the PlioMIP2 ensemble (Haywood et al., 2020; Salzmann et al., 2008) might also have contributed to the strengthening of the WAM through a vegetation feedback, which has been shown to strengthen the response of the WAM to external forcing in other past climates (e.g. Braconnot et al., 1999; Claussen and Gayler, 1997; Messori et al., 2019).

320 As the latitudinal land-ocean temperature gradient is central to the development and strength of the WAM through the development of the Saharan Heat Low (Lavaysse et al., 2009), the results have strong implications for future scenarios. Unlike the results in PlioMIP2, and previously in PlioMIP1 (Zhang et al., 2016), which exhibit a uniform rainfall increase over West Africa, both CMIP3 (SRES A2) and CMIP5 (RCP8.5) model ensembles show a drying over western Sahel and a rainfall increase over central and eastern Sahel (Roehrig et al., 2013). As analysis of both

325 CMIP3 and CMIP5 ensembles show a large spread in projected rainfall change in the Sahel region which weakens its confidence in future projections (Roehrig et al., 2013), our results support a future strengthening of the WAM and rainfall increase over West Africa and Sahel in a high $CO_2$ scenario.

5. Conclusion

The PlioMIP2 ensemble shows a clear rainfall increase over West Africa, with the largest increase located over

330 Sahel, and a strengthening of the WAM leading to the rainfall reaching farther in over the continent. These results

are consistent with geological evidence which suggests a more humid climate during the mid-Pliocene (Kuechler et al., 2018; Salzmann et al., 2008). Some regional differences occur among the ensembles, mainly along the coast of Guinea where some models indicate drier conditions while other indicate a rainfall increase. The largest inter-model variability is centered along Sahel, where the magnitude of the rainfall increase varies largely between the

335    models. The strengthened WAM is driven by the warming of the Sahara region and subsequent deepening of the Saharan Heat Low, most likely due to the greenhouse gas forcing and land/ocean warming contrast. The deepened Saharan Heat Low leads to anomalous cyclonic flow and increased moisture flux into the Sahel region, resulting in a northward shift and intensification of the rainbelt. Given the potential for using the PlioMIP2 as an analogue for near-future scenarios, these results suggest a more uniform rainfall increase over West Africa and the Sahel

340    region, unlike the east-west contrast seen in both CMIP3 and CMIP5 future projections (Roehrig et al., 2013).

*Data availability.* The model data can be downloaded from PlioMIP2 data server located at the School of Earth and Environment of the University of Leeds, an email can be sent to Alan Haywood (a.m.haywood@leeds.ac.uk) for access.

*Author contributions.* Ellen Berntell and Qiong Zhang designed the work, Ellen Berntell did the analysis and
345    wrote the manuscript. All co-authors provided the PlioMIP2 model data and commented on the manuscript.

*Competing interests.* The authors declare that they have no conflict of interest.

*Acknowledgements.* This research has been supported by the Swedish Research Council (Vetenskapsrådet, grant no. 2013-06476 and 2017-04232). The model simulations with EC-Earth3 and data analysis were performed by resources provided by ECMWF's computing and archive facilities and the Swedish National Infrastructure for Computing (SNIC) at the National
350    Supercomputer Centre (NSC) partially funded by the Swedish Research Council through grant agreement no. 2016-07213. GL and CS acknowledge computational resources from the Computing and Data Centre of the Alfred-Wegener-Institute – Helmholtz-Centre for 460 Polar and Marine Research towards generation of the COSMOS PlioMIP2 simulation ensemble. GL acknowledges funding by the Alfred Wegener Institute's research programme PACES2. CS acknowledges funding via the Helmholtz Climate Initiative REKLIM and the Alfred Wegener Institute's research programme PACES2.

355

References:

Badger, M. P. S., Schmidt, D. N., Mackensen, A. and Pancost, R. D.: High-resolution alkenone palaeobarometry indicates relatively stable pco2 during the pliocene (3.3-2.8 ma), Philos. Trans. R. Soc. A Math. Phys. Eng. Sci.,
360    371(2001), doi:10.1098/rsta.2013.0094, 2013.

Bartoli, G., Hönisch, B. and Zeebe, R. E.: Atmospheric CO2 decline during the Pliocene intensification of Northern Hemisphere glaciations, Paleoceanography, 26(4), 1–14, doi:10.1029/2010PA002055, 2011.

Berntell, E., Zhang, Q., Chafik, L. and Körnich, H.: Representation of Multidecadal Sahel Rainfall Variability in 20th Century Reanalyses, Sci. Rep., 8(1), 6–13, doi:10.1038/s41598-018-29217-9, 2018.

365    Biasutti, M., Held, I. M., Sobel, A. H. and Giannini, A.: SST forcings and Sahel rainfall variability in simulations of the twentieth and twenty-first centuries, J. Clim., 21(14), 3471–3486, doi:10.1175/2007JCLI1896.1, 2008.

Boer, G. J.: The ratio of land to ocean temperature change under global warming, Clim. Dyn., 37(11–12), 2253–2270, doi:10.1007/s00382-011-1112-3, 2011.

Bonnefille, R.: Cenozoic vegetation, climate changes and hominid evolution in tropical Africa, Glob. Planet.
370    Change, 72(4), 390–411, doi:10.1016/j.gloplacha.2010.01.015, 2010.

Braconnot, P., Joussaume, S., Marti, O. and Noblet, N. De: Synergistic feedbacks from ocean and vegetation on the African monsoon response to mid-Holocene insolation, Geophys. Res. Lett., 26(16), 2481–2484, 1999.

Byrne, M. P. and O'Gorman, P. A.: Land-ocean warming contrast over a wide range of climates: Convective quasi-equilibrium theory and idealized simulations, J. Clim., 26(12), 4000–4016, doi:10.1175/JCLI-D-12-
375    00262.1, 2013.

Chandan, D. and Peltier, W. R.: Regional and global climate for the mid-Pliocene using the University of Toronto version of CCSM4 and PlioMIP2 boundary conditions, Clim. Past, 13(7), 919–942, doi:10.5194/cp-13-919-2017, 2017.

Chandler, M., Rind, D. and Thompson, R.: Joint investigations of the middle Pliocene climate II: GISS GCM
380    Northern Hemisphere results, Glob. Planet. Change, 9(3–4), 197–219, doi:10.1016/0921-8181(94)90016-7, 1994.

Claussen, M. and Gayler, V.: The Greening of the Sahara during the Mid-Holocene : Results of an Interactive Atmosphere-Biome Model, Glob. Ecol. Biogeogr. Lett., 6(5), 369–377, doi:10.2307/2997337, 1997.

Cook, K. H.: Climate science: The mysteries of Sahel droughts, Nat. Geosci., 1(10), 647–648, doi:10.1038/ngeo320, 2008.

385    Corvec, S. and Fletcher, C. G.: Changes to the tropical circulation in the mid-Pliocene and their implications for future climate, Clim. Past, 13(2), 135–147, doi:10.5194/cp-13-135-2017, 2017.

deMenocal, P. B.: African climate change and faunal evolution during the Pliocene-Pleistocene, Earth Planet. Sci. Lett., 220(1–2), 3–24, doi:10.1016/S0012-821X(04)00003-2, 2004.

Dowsett, H., Robinson, M., Haywood, A. M., Salzmann, U., Hill, D., Sohl, L. E., Chandler, M., Williams, M.,

390    Foley, K. and Stoll, D. K.: The PRISM3D paleoenvironmental reconstruction, Stratigraphy, 7(2–3), 123–139 [online] Available from: http://pubs.er.usgs.gov/publication/70044350, 2010.

Dowsett, H. J., Foley, K. M., Stoll, D. K., Chandler, M. A., Sohl, L. E., Bentsen, M., Otto-Bliesner, B. L., Bragg, F. J., Chan, W. Le, Contoux, C., Dolan, A. M., Haywood, A. M., Jonas, J. A., Jost, A., Kamae, Y., Lohmann, G., Lunt, D. J., Nisancioglu, K. H., Abe-Ouchi, A., Ramstein, G., Riesselman, C. R., Robinson, M. M., Rosenbloom,

395    N. A., Salzmann, U., Stepanek, C., Strother, S. L., Ueda, H., Yan, Q. and Zhang, Z.: Sea surface temperature of the mid-piacenzian ocean: A data-model comparison, Sci. Rep., 3, 1–8, doi:10.1038/srep02013, 2013.

Feakins, S. J., deMenocal, P. B. and Eglinton, T. I.: Biomarker records of late Neogene changes in northeast African vegetation, Geology, 33(12), 977–980, doi:10.1130/G21814.1, 2005.

Feng, R., Otto-Bliesner, B. L., Brady, E. C. and Rosenbloom, N.: Increased Climate Response and Earth System

400    Sensitivity From CCSM4 to CESM2 in Mid-Pliocene Simulations, J. Adv. Model. Earth Syst., 12(8), doi:10.1029/2019MS002033, 2020.

Gaetani, M., Messori, G., Zhang, Q., Flamant, C. and Pausata, F. S. R.: Understanding the mechanisms behind the northward extension of the West African monsoon during the mid-holocene, J. Clim., 30(19), 7621–7642, doi:10.1175/JCLI-D-16-0299.1, 2017.

405    Giannini, A., Saravanan, R. and Chang, P.: Oceanic Forcing of Sahel Rainfall on Interannual to Interdecadal Time Scales, Science (80-. )., 302(5647), 1027–1030, doi:DOI: 10.1126/science.1089357, 2003.

Harris, I., Osborn, T. J., Jones, P. and Lister, D.: Version 4 of the CRU TS monthly high-resolution gridded multivariate climate dataset, Sci. Data, 7(1), 1–18, doi:10.1038/s41597-020-0453-3, 2020.

Haywood, A., Tindall, J., Dowsett, H., Dolan, A., Foley, K., Hunter, S., Hill, D., Chan, W.-L., Abe-Ouchi, A.,

410    Stepanek, C., Lohmann, G., Chandan, D., Peltier, W., Tan, N., Contoux, C., Ramstein, G., Li, X., Zhang, Z., Guo, C., Nisancioglu, K., Zhang, Q., Li, Q., Kamae, Y., Chandler, M., Sohl, L., Otto-Bliesner, B., Feng, R., Brady, E.,

Von der Heydt, A., Baatsen, M. and Lunt, D.: A return to large-scale features of Pliocene climate: the Pliocene Model Intercomparison Project Phase 2, Clim. Past, (January), doi:10.5194/cp-2019-145, 2020.

Haywood, A. M. and Valdes, P. J.: Modelling Pliocene warmth: Contribution of atmosphere, oceans and

415     cryosphere, Earth Planet. Sci. Lett., 218(3–4), 363–377, doi:10.1016/S0012-821X(03)00685-X, 2004.

Haywood, A. M., Dowsett, H. J., Otto-Bliesner, B., Chandler, M. A., Dolan, A. M., Hill, D. J., Lunt, D. J., Robinson, M. M., Rosenbloom, N., Salzmann, U. and Sohl, L. E.: Pliocene model intercomparison project (PlioMIP): Experimental design and boundary conditions (Experiment 1), Geosci. Model Dev., 3(1), 227–242, doi:10.5194/gmd-3-227-2010, 2010.

420     Haywood, A. M., Dowsett, H. J., Robinson, M. M., Stoll, D. K., Dolan, A. M., Lunt, D. J., Otto-Bliesner, B. and Chandler, M. A.: Pliocene Model Intercomparison Project (PlioMIP): experimental design and boundary conditions (Experiment 2), Geosci. Model Dev., 4(3), 571–577, doi:10.5194/gmd-4-571-2011, 2011.

Haywood, A. M., Hill, D. J., Dolan, A. M., Otto-Bliesner, B. L., Bragg, F., Chan, W. L., Chandler, M. A., Contoux, C., Dowsett, H. J., Jost, A., Kamae, Y., Lohmann, G., Lunt, D. J., Abe-Ouchi, A., Pickering, S. J.,

425     Ramstein, G., Rosenbloom, N. A., Salzmann, U., Sohl, L., Stepanek, C., Ueda, H., Yan, Q. and Zhang, Z.: Large-scale features of Pliocene climate: Results from the Pliocene Model Intercomparison Project, Clim. Past, 9(1), 191–209, doi:10.5194/cp-9-191-2013, 2013.

Haywood, A. M., Dowsett, H. J., Dolan, A. M., Rowley, D., Abe-Ouchi, A., Otto-Bliesner, B., Chandler, M. A., Hunter, S. J., Lunt, D. J., Pound, M. and Salzmann, U.: The Pliocene Model Intercomparison Project (PlioMIP)

430     Phase 2: Scientific objectives and experimental design, Clim. Past, 12(3), 663–675, doi:10.5194/cp-12-663-2016, 2016.

Held, I. M., Delworth, T. L., Lu, J., Findell, K. L. and Knutson, T. R.: Simulation of Sahel drought in the 20th and 21st centuries, Proc. Natl. Acad. Sci. USA, 102(50), 2005.

Hunter, S. J., Haywood, A. M., Dolan, A. M. and Tindall, J. C.: The HadCM3 contribution to PlioMIP phase 2,

435     Clim. Past, 15(5), 1691–1713, doi:10.5194/cp-15-1691-2019, 2019.

Jiang, D., Wang, H., Ding, Z., Lang, X. and Drange, H.: Modeling the middle Pliocene climate with a global

atmospheric general circulation model, J. Geophys. Res. D Atmos., 110(14), 1–14, doi:10.1029/2004JD005639, 2005.

Kamae, Y., Yoshida, K. and Ueda, H.: Sensitivity of Pliocene climate simulations in MRI-CGCM2.3 to
440    respective boundary conditions, Clim. Past, 12(8), 1619–1634, doi:10.5194/cp-12-1619-2016, 2016.

Kuechler, R. R., Dupont, L. M. and Schefuß, E.: Hybrid insolation forcing of Pliocene monsoon dynamics in West Africa, Clim. Past, 14(1), 73–84, doi:10.5194/cp-14-73-2018, 2018.

Lambert, F. H., Webb, M. J. and Joshi, M. M.: The relationship between land-ocean surface temperature contrast and radiative forcing, J. Clim., 24(13), 3239–3256, doi:10.1175/2011JCLI3893.1, 2011.

445    Lavaysse, C., Flamant, C., Janicot, S., Parker, D. J., Lafore, J.-P., Sultan, B. and Pelon, J.: Seasonal evolution of the West African heat low: a climatological perspective, Clim. Dyn., 33(2), 313–330, doi:10.1007/s00382-009-0553-4, 2009.

Li, X., Jiang, D., Tian, Z. and Yang, Y.: Mid-Pliocene global land monsoon from PlioMIP1 simulations, Palaeogeogr. Palaeoclimatol. Palaeoecol., 512(March), 56–70, doi:10.1016/j.palaeo.2018.06.027, 2018.

450    Li, X., Guo, C., Zhang, Z., Helge Otterä, O. and Zhang, R.: PlioMIP2 simulations with NorESM-L and NorESM1-F, Clim. Past, 16(1), 183–197, doi:10.5194/cp-16-183-2020, 2020.

Lurton, T., Balkanski, Y., Bastrikov, V., Bekki, S., Bopp, L., Braconnot, P., Brockmann, P., Cadule, P., Contoux, C., Cozic, A., Cugnet, D., Dufresne, J. L., Éthé, C., Foujols, M. A., Ghattas, J., Hauglustaine, D., Hu, R. M., Kageyama, M., Khodri, M., Lebas, N., Levavasseur, G., Marchand, M., Ottlé, C., Peylin, P., Sima, A., Szopa, S.,
455    Thiéblemont, R., Vuichard, N. and Boucher, O.: Implementation of the CMIP6 Forcing Data in the IPSL-CM6A-LR Model, J. Adv. Model. Earth Syst., 12(4), 1–22, doi:10.1029/2019MS001940, 2020.

Martínez-Botí, M. A., Foster, G. L., Chalk, T. B., Rohling, E. J., Sexton, P. F., Lunt, D. J., Pancost, R. D., Badger, M. P. S. and Schmidt, D. N.: Plio-Pleistocene climate sensitivity evaluated using high-resolution CO2 records, Nature, 518(7537), 49–54, doi:10.1038/nature14145, 2015.

460    Mba, W. P., Longandjo, G. N. T., Moufouma-Okia, W., Bell, J. P., James, R., Vondou, D. A., Haensler, A., Fotso-Nguemo, T. C., Guenang, G. M., Tchotchou, A. L. D., Kamsu-Tamo, P. H., Takong, R. R., Nikulin, G.,

Lennard, C. J. and Dosio, A.: Consequences of 1.5 °c and 2 °c global warming levels for temperature and precipitation changes over Central Africa, Environ. Res. Lett., 13(5), doi:10.1088/1748-9326/aab048, 2018.

Messori, G., Gaetani, M., Zhang, Q., Zhang, Q. and Pausata, F. S. R.: The water cycle of the mid-Holocene West

465     African monsoon: The role of vegetation and dust emission changes, Int. J. Climatol., 39(4), 1927–1939, doi:10.1002/joc.5924, 2019.

Mohino, E., Janicot, S. and Bader, J.: Sahel rainfall and decadal to multi-decadal sea surface temperature variability, Clim. Dyn., 37(3), 419–440, doi:10.1007/s00382-010-0867-2, 2011.

Nicholson, S. E., Some, B. and Kone, B.: An analysis of recent rainfall conditions in West Africa, including the

470     rainy seasons of the 1997 El Nino and the 1998 La Nina years, J. Clim., 13(14), 2628–2640, doi:10.1175/1520-0442(2000)013<2628:AAORRC>2.0.CO;2, 2000.

De Nooijer, W., Zhang, Q., Li, Q., Zhang, Q., Li, X., Zhang, Z., Guo, C., Nisancioglu, K. H., Haywood, A. M., Tindall, J. C., Hunter, S. J., Dowsett, H. J., Stepanek, C., Lohmann, G., Otto-bliesner, B. L., Feng, R., Linda, E., Tan, N., Contoux, C., Ramstein, G., Baatsen, M. L. J. and Der, A. S. Von: Evaluation of Arctic warming in mid-

475     Pliocene climate simulations, Clim. Past, 2(May), 1–30, 2020.

Otto-Bliesner, B. L., Brady, E. C., Zhao, A., Brierley, C., Axford, Y., Capron, E., Govin, A., Hoffman, J., Isaacs, E., Kageyama, M., Scussolini, P., Tzedakis, P. C., Williams, C., Wolff, E., Abe-Ouchi, A., Braconnot, P., Ramos Buarque, S., Cao, J., de Vernal, A., Guarino, M. V, Guo, C., LeGrande, A. N., Lohmann, G., Meissner, K., Menviel, L., Nisancioglu, K., O'ishi, R., Salas Y Melia, D., Shi, X., Sicard, M., Sime, L., Tomas, R., Volodin, E.,

480     Yeung, N., Zhang, Q., Zhang, Z. and Zheng, W.: Large-scale features of Last Interglacial climate: Results from evaluating the \textit{lig127k} simulations for CMIP6-PMIP4, Clim. Past Discuss., 2020, 1–41, doi:10.5194/cp-2019-174, 2020.

Pagani, M., Liu, Z., Lariviere, J. and Ravelo, A. C.: High Earth-system climate sensitivity determined from Pliocene carbon dioxide concentrations, Nat. Geosci., 3(1), 27–30, doi:10.1038/ngeo724, 2010.

485     Pontes, G. M., Wainer, I., Taschetto, A. S., Gupta, A. Sen, Ouchi, A. A., Brady, E. C., Chan, W. Le, Chandan, D., Contoux, C., Feng, R., Hunter, S. J., Kame, Y., Lohmann, G., Bliesner, B. L. O., Peltier, W. R., Stepanek, C., Tindall, J., Tan, N. and Zhang, Q.: Drier tropical and subtropical Southern Hemisphere in the mid - Pliocene

Warm Period, Sci. Rep., 1–11, doi:10.1038/s41598-020-68884-5, 2020.

Raymo, M. E., Grant, B., Horowitz, M. and Rau, G. H.: Mid-Pliocene warmth: Stronger greenhouse and stronger

490    conveyor, Mar. Micropaleontol., 27(1–4), 313–326, doi:10.1016/0377-8398(95)00048-8, 1996.

Roehrig, R., Bouniol, D., Guichard, F., Hourdin, F. déric and Redelsperger, J. L.: The present and future of the

west african monsoon: A process-oriented assessment of CMIP5 simulations along the AMMA transect, J. Clim.,

26(17), 6471–6505, doi:10.1175/JCLI-D-12-00505.1, 2013.

Salzmann, U., Haywood, A. M., Lunt, D. J., Valdes, P. J. and Hill, D. J.: A new global biome reconstruction and

495    data-model comparison for the Middle Pliocene, Glob. Ecol. Biogeogr., 17(3), 432–447, doi:10.1111/j.1466-

8238.2008.00381.x, 2008.

Salzmann, U., Dolan, A. M., Haywood, A. M., Chan, W. Le, Voss, J., Hill, D. J., Abe-Ouchi, A., Otto-Bliesner,

B., Bragg, F. J., Chandler, M. A., Contoux, C., Dowsett, H. J., Jost, A., Kamae, Y., Lohmann, G., Lunt, D. J.,

Pickering, S. J., Pound, M. J., Ramstein, G., Rosenbloom, N. A., Sohl, L., Stepanek, C., Ueda, H. and Zhang, Z.:

500    Challenges in quantifying Pliocene terrestrial warming revealed by data-model discord, Nat. Clim. Chang., 3(11),

969–974, doi:10.1038/nclimate2008, 2013.

Samakinwa, E., Stepanek, C. and Lohmann, G.: Sensitivity of mid-Pliocene climate to changes in orbital forcing,

and PlioMIP's boundary conditions, Clim. Past Discuss., 1(January), 1–35, doi:10.5194/cp-2020-5, 2020.

Schulzweida, U.: CDO User Guide (Version 1.9.8), Zendo, (October) [online] Available from:

505    http://doi.org/10.5281/zenodo.3539275, 2019.

Seki, O., Foster, G. L., Schmidt, D. N., Mackensen, A., Kawamura, K. and Pancost, R. D.: Alkenone and boron-

based Pliocene pCO2 records, Earth Planet. Sci. Lett., 292(1–2), 201–211, doi:10.1016/j.epsl.2010.01.037, 2010.

Stepanek, C., Samakinwa, E. and Lohmann, G.: Contribution of the coupled atmosphere–ocean–sea ice–

vegetation model COSMOS to the PlioMIP2, Clim. Past Discuss., (February), 1–72, doi:10.5194/cp-2020-10,

510    2020.

Sun, Y., Ramstein, G., Contoux, C. and Zhou, T.: A comparative study of large-scale atmospheric circulation in

the context of a future scenario (RCP4.5) and past warmth (mid-Pliocene), Clim. Past, 9(4), 1613–1627,

doi:10.5194/cp-9-1613-2013, 2013.

Sutton, R. T., Dong, B. and Gregory, J. M.: Land/sea warming ratio in response to climate change: IPCC AR4

515    model results and comparison with observations, Geophys. Res. Lett., 34(2), 2–6, doi:10.1029/2006GL028164,

2007.

Tan, N., Contoux, C., Ramstein, G., Sun, Y., Dumas, C., Sepulchre, P. and Guo, Z.: Modeling a modern-like

pCO_2 warm period (Marine Isotope Stage KM5c) with two versions of an Institut Pierre Simon Laplace

atmosphere--ocean coupled general circulation model, Clim. Past, 16(1), 1–16, doi:10.5194/cp-16-1-2020, 2020.

520    Tripati, A. K., Roberts, C. D. and Eagle, R. A.: Coupling of CO2 and Ice sheet stability over major climate

transitions of the last 20 million years, Science (80-. )., 326(5958), 1394–1397, doi:10.1126/science.1178296,

2009.

Wan, S., Tian, J., Steinke, S., Li, A. and Li, T.: Evolution and variability of the East Asian summer monsoon

during the Pliocene: Evidence from clay mineral records of the South China Sea, Palaeogeogr. Palaeoclimatol.

525    Palaeoecol., 293(1–2), 237–247, doi:10.1016/j.palaeo.2010.05.025, 2010.

Williams, K. D., Copsey, D., Blockley, E. W., Bodas-Salcedo, A., Calvert, D., Comer, R., Davis, P., Graham, T.,

Hewitt, H. T., Hill, R., Hyder, P., Ineson, S., Johns, T. C., Keen, A. B., Lee, R. W., Megann, A., Milton, S. F.,

Rae, J. G. L., Roberts, M. J., Scaife, A. A., Schiemann, R., Storkey, D., Thorpe, L., Watterson, I. G., Walters, D.

N., West, A., Wood, R. A., Woollings, T. and Xavier, P. K.: The Met Office Global Coupled Model 3.0 and 3.1

530    (GC3.0 and GC3.1) Configurations, J. Adv. Model. Earth Syst., 10(2), 357–380, doi:10.1002/2017MS001115,

2018.

Zhang, R., Zhang, Z., Jiang, D., Yan, Q., Zhou, X. and Cheng, Z.: Strengthened African summer monsoon in the

mid-Piacenzian, Adv. Atmos. Sci., 33(9), 1061–1070, doi:10.1007/s00376-016-5215-y, 2016.

Zhang, Y. G., Pagani, M., Liu, Z., Bohaty, S. M. and Deconto, R.: A 40-million-year history of atmospheric CO

535    2. Phil Trans R Soc A A 40-million-year history of atmospheric CO 2, , (September),

doi:10.1098/rsta.2013.0096, 2013.